Eur. Phys. J. E (2018) **41**: 115
DOI 10.1140/epje/i2018-11726-4

THE EUROPEAN PHYSICAL JOURNAL E

Regular Article

Particle-laden two-dimensional elastic turbulence*

Himani Garg[a], Enrico Calzavarini, Gilmar Mompean, and Stefano Berti

Université de Lille, Unité de Mécanique de Lille, UML EA 7512, F-59000 Lille, France

Received 31 March 2018 and Received in final form 19 July 2018
Published online: 2 October 2018

Abstract. The aggregation properties of heavy inertial particles in the elastic turbulence regime of an Oldroyd-B fluid with periodic Kolmogorov mean flow are investigated by means of extensive numerical simulations in two dimensions. Both the small- and large-scale features of the resulting inhomogeneous particle distribution are examined, focusing on their connection with the properties of the advecting viscoelastic flow. We find that particles preferentially accumulate on thin highly elastic propagating structures and that this effect is the largest for intermediate values of particle inertia. We provide a quantitative characterization of this phenomenon that allows to relate it to the accumulation of particles in filamentary highly strained flow regions producing clusters of correlation dimension close to 1. At larger scales, particles are found to undergo turbophoretic-like segregation. Indeed, our results indicate a close relationship between the profiles of particle density and fluid velocity fluctuations. The large-scale inhomogeneity of the particle distribution is interpreted in the framework of a model derived in the limit of small, but finite, particle inertia. The qualitative characteristics of different observables are, to a good extent, independent of the flow elasticity. When increased, the latter is found, however, to slightly reduce the globally averaged degree of turbophoretic unmixing.

1 Introduction

Viscoelastic fluids are known to be characterized by non-Newtonian behavior under appropriate conditions. In particular, dilute polymer solutions may display non-negligible elastic forces when the suspended polymeric chains occur to be sufficiently stretched by fluid velocity gradients. Remarkably, when the elasticity of the solution overcomes a critical value such forces can trigger instabilities that can eventually lead to irregular turbulent-like flow, even in the absence of fluid inertia, namely in the limit of vanishing Reynolds number. The latter dynamical regime is known as elastic turbulence [1] and it has been experimentally observed in different flow configurations [1–5]. On the basis of its similarity with turbulent fluid motion, elastic turbulence has been proposed as an efficient system to enhance mixing in low Reynolds number flows [2]. Moreover, it has been shown that it can increase heat transfer [6, 7] and promote emulsification [8]. Recently, it has also been argued that elastic turbulence flows play a significant role in the increased oil displacement obtained in industrial processes employing dilute polymer solutions to flood porous reservoir rocks [9].

Transport and mixing processes in fluids, however, often involve the presence of suspended finite-size impurities, like small and heavy solid particles. In view of mixing applications in elastic turbulence flows, it then seems necessary to accurately characterize how particle inertia affects the concentration of the transported species. Indeed, it is known that in turbulent flows the difference between the mass density of the impurities and that of the carrier fluid typically induces unmixing effects. Namely, it produces non-homogeneous particle distributions at small scales, as well as at large ones when turbulence spatial inhomogeneities are present (as, *e.g.*, in a duct or in a boundary-layer flow). Although both types of inhomogeneities can be simultaneously present, they correspond to essentially different phenomena. While at small scales they give rise to complex clustered distributions due to the combined effect of small-scale turbulence and particle inertia [10], at large scales they manifest in the accumulation of particles in regions of minimal turbulent intensity, whose locations are tightly related to the structure of the mean flow (turbophoresis) [11–14].

Inertial particle dynamics have been studied in turbulent flows of both Newtonian (see, *e.g.*, [10, 15–17]) and non-Newtonian (*e.g.*, in [18, 19]) fluids. The present work

* Contribution to the Topical Issue "Flowing Matter, Problems and Applications", edited by Federico Toschi, Ignacio Pagonabarraga Mora, Nuno Araujo, Marcello Sega.

[a] e-mail: himani.garg@etudiant.univ-lille1.fr

reports an investigation of heavy inertial particle transport at low Reynolds number, in a non-homogeneous flow of elastic turbulence in two dimensions. Despite the potential of the latter for mixing in microfluidics, the dynamics of particles in this regime are still quite unexplored, but see [20]. Our goal is to study the statistical features of particle aggregation at both small and large scales, and to relate them to the behavior of the main observables associated with the dynamics of the viscoelastic flow, as polymer elongation and velocity fluctuations, and to flow structures.

The paper is organized as follows. The model used to describe the dynamics of heavy particles in a viscoelastic flow that can develop elastic turbulence states is introduced in sect. 2. In sect. 3 we present the results of numerical simulations of this model. After briefly illustrating the main properties of the flow fields (sect. 3.1), we report on the properties of particle spatial distributions, separately focusing on preferential concentration effects (sect. 3.2), small-scale fractal clustering (sect. 3.3) and large-scale inhomogeneities, *i.e.* turbophoresis (sect. 3.4). Conclusions are presented in sect. 4.

2 Model of particle-laden viscoelastic flows

We consider the dynamics of a dilute polymer solution as described by the Oldroyd-B model [21]:

$$\partial_t \boldsymbol{u} + (\boldsymbol{u}\cdot\boldsymbol{\nabla})\boldsymbol{u} = -\frac{\boldsymbol{\nabla} p}{\rho_f} + \nu_s \Delta \boldsymbol{u} + \frac{2\eta\nu_s}{\tau}\boldsymbol{\nabla}\cdot\boldsymbol{\sigma} + \boldsymbol{f}, \quad (1)$$

$$\partial_t \boldsymbol{\sigma} + (\boldsymbol{u}\cdot\boldsymbol{\nabla})\boldsymbol{\sigma} = (\boldsymbol{\nabla}\boldsymbol{u})^T\cdot\boldsymbol{\sigma} + \boldsymbol{\sigma}\cdot(\boldsymbol{\nabla}\boldsymbol{u}) - 2\frac{\boldsymbol{\sigma}-\mathbf{1}}{\tau}. \quad (2)$$

In the above equations $\boldsymbol{u}$ is the incompressible velocity field, the symmetric positive definite matrix $\boldsymbol{\sigma}$ represents the normalized conformation tensor of polymer molecules and $\mathbf{1}$ is the unit tensor corresponding to the equilibrium configuration of polymers attained in the absence of flow ($\boldsymbol{u}=0$). The trace $\mathrm{tr}(\boldsymbol{\sigma})$ gives the local polymer (square) elongation and τ is the largest polymer relaxation time. The fluid density is denoted ρ_f and the total viscosity of the solution is $\nu = \nu_s(1+\eta)$, with ν_s the kinematic viscosity of the solvent and η the zero-shear contribution of polymers (which is proportional to polymer concentration). The extra stress term $\frac{2\eta\nu_s}{\tau}\boldsymbol{\nabla}\cdot\boldsymbol{\sigma}$ accounts for elastic forces providing a feedback mechanism on the flow.

In this study we are interested in having a fluid velocity characterized by a non-homogenous mean flow and turbulent fluctuations generated by elastic stresses only. For this reason we choose the two-dimensional (2D) periodic viscoelastic Kolmogorov flow. This has been previously shown [22–24] to provide a simple and effective model able to reproduce the basic phenomenology of elastic turbulence. Using the Kolmogorov forcing $\boldsymbol{f} = (F\cos(y/L), 0)$ in eq. (1), one has a laminar fixed point corresponding to the velocity field $\boldsymbol{u}^{(0)} = (U_0\cos(y/L), 0)$ and the conformation tensor components $\sigma_{11}^{(0)} = 1 + \frac{\tau^2 U_0^2}{2L^2}\sin^2(y/L)$, $\sigma_{12}^{(0)} = \sigma_{21}^{(0)} = -\frac{\tau U_0}{2L}\sin(y/L)$, $\sigma_{22}^{(0)} = 1$, with $F = \nu U_0/L^2$ [25]. From these expressions, characteristic length and velocity scales L and U_0, respectively, can be identified. As previously documented, the laminar flow becomes unstable [25] for sufficiently high values of elasticity, even in the absence of fluid inertia, and eventually displays features typical of turbulent flows [22–24]. In the elastic turbulence regime, the mean velocity and conformation tensor fields keep similar trigonometric functional forms but with different amplitudes. Denoting U the mean velocity amplitude in such states, we define the Reynolds number as $Re = UL/\nu$ and the Weissenberg number as $Wi = U\tau/L$, with their ratio giving the elasticity $El = Wi/Re$ of the flow.

We assume that small spherical particles heavier than the fluid are laden in flows ruled by the dynamics described above. The suspension of impurities is considered to be dilute. The only force experienced by particles is Stokes drag and we then do not take into account the feedback effect of particles on the advecting fluid velocity and interactions among particles. Under these hypotheses the dynamics of each particle is described by the following equations of motion [26] for their position $\boldsymbol{x}$ and velocity $\boldsymbol{v}$:

$$\dot{\boldsymbol{x}} = \boldsymbol{v}, \quad (3)$$

$$\dot{\boldsymbol{v}} = -\frac{1}{\tau_p}\left[\boldsymbol{v} - \boldsymbol{u}(\boldsymbol{x},t)\right], \quad (4)$$

where $\tau_p = \frac{2a_p^2\rho_p}{9\nu\rho_f}$ is the Stokes time, accounting for particle inertia, a_p the particle radius, ρ_p particle density (with $\rho_p \gg \rho_f$) and $\boldsymbol{u}(\boldsymbol{x},t)$ the advecting flow resulting from eqs. (1) and (2). Particle inertia is typically parametrized by the Stokes number $St = \tau_p/\tau_f$ with τ_f a characteristic flow time scale. Here we define $\tau_f \equiv \tau_{\dot\gamma}$ in terms of the strain rate exerted by the flow, so that $St = \tau_p/\tau_{\dot\gamma}$, with $\tau_{\dot\gamma} = 1/\overline{\dot\gamma}$ and $\overline{\dot\gamma}$ given by

$$\overline{\dot\gamma} = \frac{1}{TL_0^2}\int_0^T \mathrm{d}t \int_0^{L_0}\mathrm{d}y\int_0^{L_0}\mathrm{d}x\sqrt{2[\boldsymbol{\nabla}\boldsymbol{u} + (\boldsymbol{\nabla}\boldsymbol{u})^T]^2}, \quad (5)$$

where $\overline{(\ldots)}$ represents an average over spatial coordinates and time, L_0 being the domain size in each direction.

3 Analysis and results

To explore the dynamics of inertial particles in elastic turbulence we perform direct numerical simulations. Equations (1) and (2) are integrated using a pseudospectral method on a grid of side $L_0 = 2\pi$ with periodic boundary conditions at resolution 512^2. Integration of viscoelastic models is limited by instabilities associated with the loss of positiveness of the conformation tensor [27]. These instabilities are particularly relevant at high Wi values and limit the possibility to numerically investigate the elastic turbulence regime by direct implementation of the equations of motion. For this reason we adopt an algortithm based on a Cholesky decomposition of the conformation matrix ensuring symmetry and positive definiteness [28];

to stabilize the code a small polymer diffusivity, corresponding to a Schmidt number $Sc \simeq 10^3$, was also added. This approach allows us to reach sufficiently high elasticity; however it imposes some limitations in terms of resolution and computational time. We fix $Re = 1$ (using the value of U_0 to obtain an *a priori* estimate of it), which is smaller than the critical value $\sqrt{2}$ of the Newtonian case, and we vary Wi in a range of values larger than a critical one $Wi_c \approx 10$ corresponding to the onset of purely elastic instabilities [23]. In all simulations the other parameters of the viscoelastic dynamics are $U_0 = 4$, $L = 1/4$, $\nu_s = 0.769$, $\eta = 0.3$. The initial condition is obtained by adding a small random perturbation to the fixed point solution $\boldsymbol{u}^{(0)}$, $\boldsymbol{\sigma}^{(0)}$ and the system is evolved in time until a statistically steady state is reached.

Once the flow is in statistically stationary conditions, it is seeded with an ensemble of inertial particles, initially uniformly distributed in space and having randomly chosen velocities. Particle dynamics, eqs. (3) and (4), are integrated by means of a standard Lagrangian approach using a second-order Runge-Kutta time-marching scheme; the velocity at particle positions is obtained by bilinear interpolation in space. Periodic boundary conditions are imposed on particle positions. A rather large number of Stokes time (τ_p) values is examined, allowing to explore almost three decades in St (for each considered flow, *i.e.* for each Wi). In the results reported in the following sections the number of particles is $N_p = 10^4$ (tests with $N_p = 10^5$ did not show any appreciable difference on the statistics of single-particle observables).

3.1 Elastic turbulence flows

The transition from laminar to elastic turbulence states of the system specified by eqs. (1) and (2) was previously studied in detail in [23]. Notice that in the elastic turbulence regime the mean flow amplitude results to be decreased ($U < U_0$), and in the following Re and Wi will be defined using the *a posteriori* measured value U. Here we are interested in working in the regime corresponding to Weissenberg numbers well above the threshold value Wi_c; the highest Wi that we can safely reach in the present conditions is $Wi \approx 25$. For such values of Wi the flow develops temporally and spatially irregular fluctuations associated with chaotic and mixing dynamics reminiscent of turbulence. From a statistical point of view, these turbulent-like features are described by the spectra of kinetic energy $E(k)$ and of the polymer elongation, which is proportional to that of elastic energy and is given by the trace of the conformation tensor $\Sigma(k)$ at wave number k. For both quantities we find power-law behaviors as $E(k) \sim k^{-\gamma}$ (fig. 1(a)) and $\Sigma(k) \sim k^{-\delta}$ (fig. 1(b)), indicating a whole range of active scales. The kinetic energy spectrum is characterized by an exponent $3.5 < \gamma < 3.6$ larger than 3, pointing to smooth flow, and in reasonable agreement with the value measured in (three-dimensional) experiments (see, *e.g.*, [1]) and with theoretical predictions [29] based on a simplified model corresponding to the large polymer elongation limit of Oldroyd-B model.

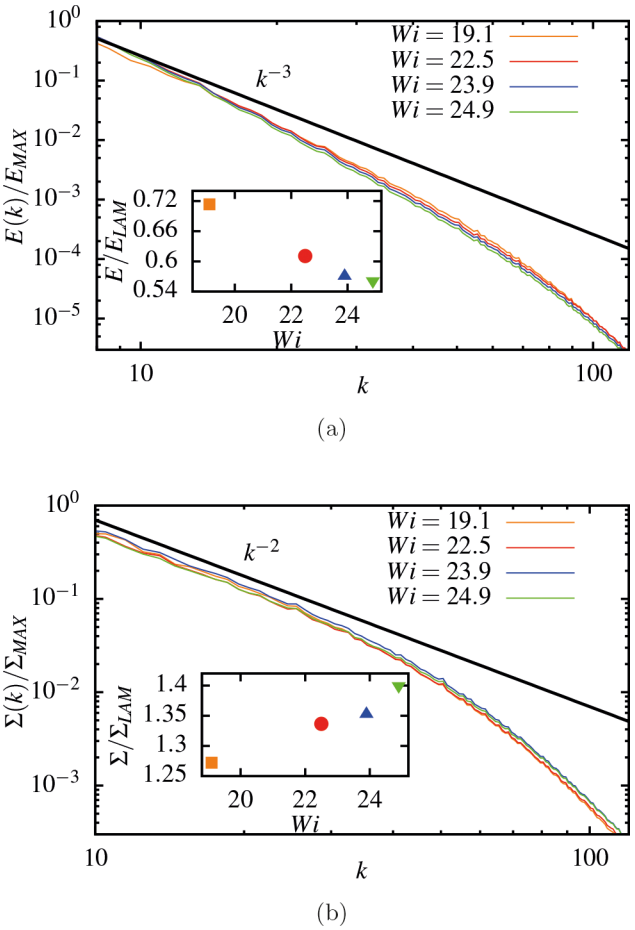

Fig. 1. Time averaged spectra of kinetic energy $E(k)$ (a) and trace of the conformation tensor $\Sigma(k)$ at wave number k (b), normalized by their maximum values, for different values of Wi in the elastic turbulence regime. Inset of panel (a): temporally averaged kinetic energy $E = \overline{|\boldsymbol{u}|^2}/2$ normalized by its laminar value $E_{LAM} = U_0^2/4$. Inset of panel (b): temporally and spatially averaged square polymer elongation $\Sigma = \overline{\mathrm{tr}(\boldsymbol{\sigma})}$ normalized by its laminar value $\Sigma_{LAM} = 2 + \frac{Wi^2}{4}$.

The spectral exponent of $\Sigma(k)$ is found to be $\delta \approx 2$, similarly to what is observed in numerical simulations of viscoelastic turbulence at higher Re (and with finite extensibility models of polymer dynamics) [30,31], and roughly in agreement with experimental results [32].

In the insets of fig. 1(a) and fig. 1(b), respectively, we report the behavior of global quantities, namely the (temporally averaged) kinetic energy $E = \overline{|\boldsymbol{u}|^2}/2$ and the (temporally averaged) trace of the conformation tensor $\Sigma = \overline{\mathrm{tr}(\boldsymbol{\sigma})}$, normalized by their laminar values $E_{LAM} = U_0^2/4$ and $\Sigma_{LAM} = 2 + Wi^2/4$, as a function of the Weissenberg number. In agreement with previous observations [22,23], we find that while the kinetic energy decreases with Wi, the square polymer elongation grows and this occurs faster than in laminar conditions. This suggests that polymers elongate by draining energy from the mean flow and, once sufficiently stretched they are capable of modifying the carrier flow through the term $\frac{2\eta\nu_s}{\tau}\boldsymbol{\nabla}\cdot\boldsymbol{\sigma}$ in eq. (1).

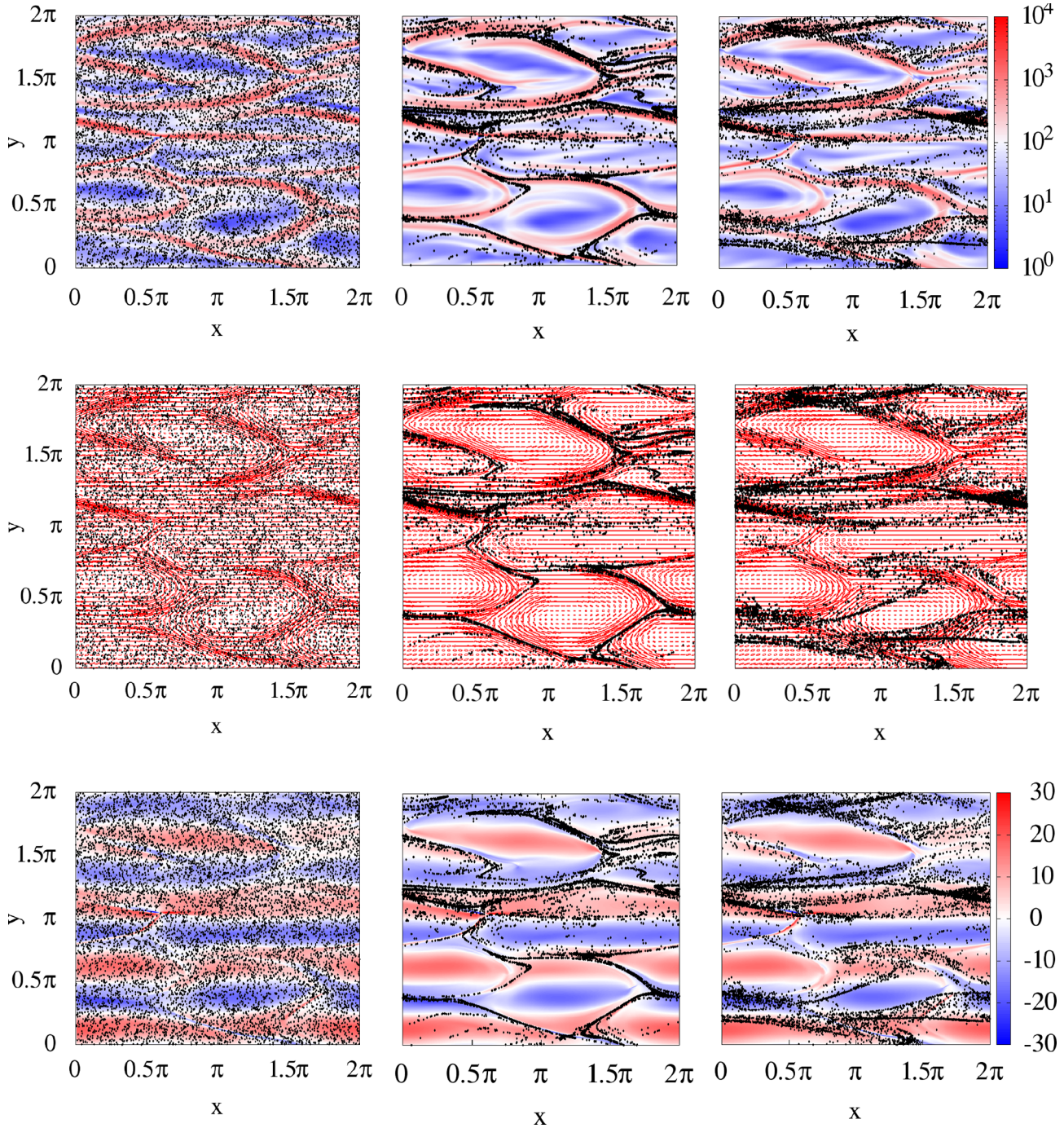

Fig. 2. Particle distribution (black dots) for $St = 0.016$, $St = 0.657$ and $St = 5.75$ (from left to right) at a fixed instant of time in statistically stationary conditions at $Wi = 23.9$ and $Re = 0.664$; the number of particles is $N_p = 10^4$. The pseudocolor plots in the upper and bottom panels, respectively, correspond to instantaneous snapshots of $[\mathrm{tr}(\boldsymbol{\sigma})](x, y)$ and vorticity $\zeta(x, y) = \boldsymbol{\nabla} \times \boldsymbol{u}(x, y)$ at the same time for which particles are plotted. In the central panel, particles are plotted together with an ellipsoid-glyph visualization of the polymer conformation tensor $\boldsymbol{\sigma}$ (with the ellipses' axes directed as the eigenvectors of $\boldsymbol{\sigma}$ and their sizes proportional to the corresponding eigenvalues).

The faster than laminar growth means that such elastic coupling is very efficient in sustaining the stretching of polymers.

3.2 Preferential concentration effects

We now discuss particle dynamics, starting from an analysis of the statistical properties of their spatial distribution in relation with the main dynamical features of the viscoelastic fluid flow. Throughout all this study $\tau_{\dot{\gamma}} \approx 0.1$ and the polymer relaxation time τ is typically larger than both $\tau_{\dot{\gamma}}$ and τ_p. As is evident from fig. 2 (where $Wi = 23.9$ and St increases from left to right), due to their inertia, particles non-homogeneously distribute in space. Let us remark, here, that Lagrangian tracers (*i.e.*, non-inertial

particles for which $St = 0$) evolve according to $\dot{\boldsymbol{x}} = \boldsymbol{u}$ (with $\boldsymbol{\nabla}\cdot\boldsymbol{u} = 0$) and, consequently, homogeneously sample the flow field over sufficiently long times. In the presence of inertia, the non-homogeneous character of the particle distribution appears to vary non-monotonically with St, with a maximum for intermediate values of this parameter. This is in agreement with intuitive expectations: for very small St one should recover tracer dynamics, while for very large St particle dynamics should be essentially insensitive to the flow. In fig. 2 both small-scale inhomogeneities and larger-scale modulations of the particle distributions are seen. A striking feature is, however, the accumulation of particles along thin filamentary structures characterized by large polymer elongations, *i.e.* large values of $\mathrm{tr}(\boldsymbol{\sigma})$ (see upper panel of fig. 2). Such highly elastic filaments, propagating along the mean flow direction, are associated with the stretching of polymers by the largest gradients of the mean velocity field [23]. Similar wavy patterns also characterize the vorticity field $\zeta = \boldsymbol{\nabla}\times\boldsymbol{u}$ (see bottom panel of fig. 2), due to the coupling between polymeric and velocity dynamics. The strong correlation between the spatial organization of the particle distribution and that of the polymer conformation tensor field is further evidenced by plotting the latter by means of an ellipsoid representation of the local (in space) principal elongations (central line of fig. 2, where the ellipses' axes are oriented as the eigenvectors of $\boldsymbol{\sigma}$ and their sizes are proportional to the corresponding eigenvalues).

In order to quantitatively assess this point, we computed the trace of the conformation tensor $\overline{\mathrm{tr}(\boldsymbol{\sigma})}$, averaged over the whole space domain and a long time history, experienced by inertial particles as a function of Stokes and for different values of Wi. The curves reported in fig. 3 have a non-monotonic behavior, with a maximum of $\overline{\mathrm{tr}(\boldsymbol{\sigma})}$ for $St \approx 1$. Their qualitative features are generic with respect to the value of the Weissenberg number. Indeed, as shown in the inset of fig. 3, after rescaling $\overline{\mathrm{tr}(\boldsymbol{\sigma})}$ with the same quantity $\overline{\mathrm{tr}(\boldsymbol{\sigma})}_{St=0}$ computed for tracers in the same flow (for each Wi) we obtain a good collapse of the data, indicating the Wi independence of this observable. These results demonstrate that when inertia is increased, and not too large, particles have an increasing tendency to concentrate where polymers are highly stretched. Moreover, as it is clear from the inset of the figure, independently of St, inertial particles experience larger values of $\mathrm{tr}(\boldsymbol{\sigma})$ than fluid-flow Lagrangian tracers.

To understand the phenomenology described above, one has to relate elastic filaments to the velocity field that transports particles. A hint in this sense comes from inspection of ellipsoid-glyph visualizations of the polymer conformation tensor (fig. 2). In these plots, the presence of regions of recirculating motion is more evident, with elastic filamentary stuctures playing the role of flow separatrices (as also observed in numerical simulations of viscoelastic cellular flows [33]). Some details on the formation of vortices in this elastic turbulence flow can be found in [23]. Here, instead, we want to focus on their impact on particle dynamics. In fact, several previous studies (see, *e.g.*, [10,34,35]) have demonstrated that small and heavy

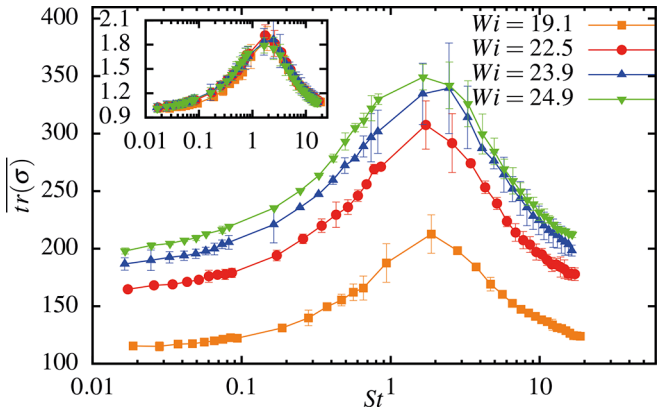

Fig. 3. Average trace of the conformation tensor $\overline{\mathrm{tr}(\boldsymbol{\sigma})}$ experienced by particles as a function of St and for different Weissenberg numbers. Here temporal averages are performed over 50 snapshots of $\mathrm{tr}(\boldsymbol{\sigma})$ (and simultaneous particle distributions) corresponding to different instants of time separated by an interval larger than the typical flow time scale. The inset shows the same after rescaling $\overline{\mathrm{tr}(\boldsymbol{\sigma})}$ with its value computed using Lagrangian tracers $\overline{\mathrm{tr}(\boldsymbol{\sigma})}_{St=0}$.

inertial particles migrate to strain dominated flow regions because they are expelled from vortical regions by centrifugal forces. At least in the small St limit, this can be explained as follows. From a Taylor expansion of eq. (4) at first order in τ_p one has $\boldsymbol{v} \simeq \boldsymbol{u} - \tau_p(\partial_t\boldsymbol{u} + \boldsymbol{u}\cdot\boldsymbol{\nabla}\boldsymbol{u})$ [34]. Then, for the divergence of the particle velocity one obtains

$$\boldsymbol{\nabla}\cdot\boldsymbol{v} = -\tau_p\,\mathrm{tr}\left[\boldsymbol{\nabla}\boldsymbol{u}\cdot(\boldsymbol{\nabla}\boldsymbol{u})^T\right], \tag{6}$$

using the incompressibility of the velocity field $\boldsymbol{u}$. Decomposing the fluid velocity gradient $\boldsymbol{\nabla}\boldsymbol{u}$ into its symmetric $\boldsymbol{S}$ and anti-symmetric part $\boldsymbol{\Omega}$, we then have

$$\boldsymbol{\nabla}\cdot\boldsymbol{v} = 2\tau_p Q, \tag{7}$$

where, up to a prefactor redefinition,

$$Q = \frac{1}{2}(\Omega_{ij}\Omega_{ij} - S_{ij}S_{ij}) \tag{8}$$

is the Okubo-Weiss parameter [36,37]. In the above equation S_{ij} and Ω_{ij}, respectively, indicate the elements of the rate-of-strain ($\boldsymbol{S}$) and rate-of-rotation ($\boldsymbol{\Omega}$) tensors, and summation over repeated indices is assumed. Particles concentrate due to (weak) compressibility of their velocity, that is where $\boldsymbol{\nabla}\cdot\boldsymbol{v} < 0$. From eq. (7) it is seen that this condition translates into negative values of Q, meaning that particles are expected to preferentially sample strain dominated regions (using eq. (8)).

Figure 4 shows the spatially and temporally averaged Okubo-Weiss parameter measured at particle positions *versus* St and for different Weissenberg numbers. The results support the above argument and provide a quantitative confirmation of what observed from fig. 2. Indeed, $\overline{Q}$ is found to be always negative, which suggests that particles are ejected from recirculating regions to get more concentrated in regions dominated by strain, where polymers are

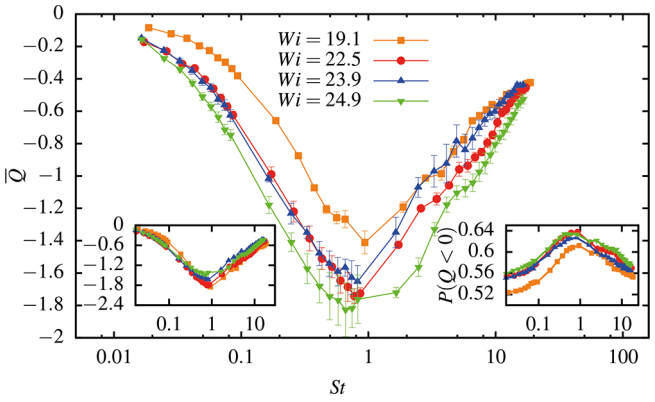

Fig. 4. Average Okubo-Weiss parameter $\overline{Q}$ experienced by particles as a function of St. Here temporal averages are performed over 50 snapshots of Q (and simultaneous particle distributions) corresponding to different instants of time separated by an interval larger than the typical flow time scale. Left inset: normalized Okubo-Weiss parameter $\overline{Q}/Q^{rms}_{St=0}$ as a function of St, where $Q^{rms}_{St=0}$ is the root-mean-square value of Q experienced by Lagrangian tracers. Right inset: probability that a particle is in strain dominated regions $P(Q<0)$ as a function of Stokes.

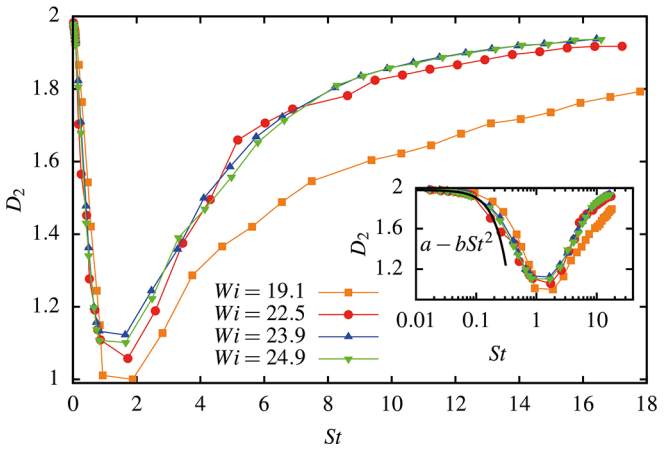

Fig. 5. Correlation dimension D_2 of particle distributions as a function of St and for different Weissenberg numbers; uncertainties are of the order of point size. Small-scale clustering is maximum for $St \sim 1$, where D_2 has a minimum. The relative difference between the values obtained for $Wi = 19.1$ and the corresponding ones for $Wi = 24.9$ is not larger than 0.15. The inset shows the same in log-linear scale; the solid line corresponds to $a - bSt^2$ with $a = 1.98$ and $b = 7.74$ after averaging the values of the fitted parameters obtained for each Wi.

highly elongated. Also in this case, the effect is maximum (*i.e.* $\overline{Q}$ is minimum) for $St \approx 1$. The effect of varying Wi is found to be quite weak. In the left inset of fig. 4 we show the behavior, *versus* St, of Okubo-Weiss parameter rescaled with its root-mean-square (rms) value computed for tracers $Q^{rms}_{St=0}$ (since $\overline{Q} = 0$ for Lagrangian tracers and, equivalently, for the Eulerian fluid flow, from numerical simulations). After rescaling, the results are only very weakly dependent on Wi. We end this section by commenting on the right inset of fig. 4. The plot presents the probability $P(Q<0)$ that a particle is in a strain dominated region, which is computed as the ratio between the number of particles at positions where $Q<0$ and the total number of particles, as a function of St. The probability $P(Q<0)$ generally takes values larger than the one realized in the limit of very small St. Despite not large, such an increase of $P(Q<0)$ indicates that inertial particles are more concentrated than tracers in regions where $Q<0$. Finally, we observe that the effect is, again, maximum for $St \approx 1$ and weakly dependent on Wi.

3.3 Correlation dimension of small-scale clusters

The previous analysis allowed us to reveal some relations between the inhomogeneities of the particle distribution and flow structures. The fine scale properties of particle clustering are, however, a more general consequence of the contraction of volumes in the phase space of the dissipative system of eqs. (3) and (4) [15]. In both laminar unsteady and turbulent flows, it has been shown that the motion of inertial particles at small scales is highly non-trivial and, at sufficiently large times, it occurs on a fractal set [15,38]. A possibility to quantitatively characterize clustering is then to measure the fractal dimension of the projection, in physical space, of the attractor of the dynamics. When this is smaller than the dimension of the full physical space, particle pairs are more likely separated by small distances. Within this framework, a common indicator is the correlation dimension D_2 [39], which is defined as

$$D_2 = \lim_{r\to 0} \frac{\log[C(r)]}{\log(r)}\,, \tag{9}$$

with the correlation sum $C(r)$ given by

$$C(r) = \lim_{N_p\to\infty} \frac{2}{N_p(N_p-1)} \sum_{i,j>i}^{N_p} \Theta(r - |\boldsymbol{x}_i - \boldsymbol{x}_j|),$$

where Θ is the Heaviside step function and $\boldsymbol{x}_i$ and $\boldsymbol{x}_j$ are the positions of particles belonging to pair (i,j). Equation (9) then means that, for small r, the probability to find particle pairs separated by a distance less than r scales as $C(r) \sim r^{D_2}$.

The behavior of D_2 as a function of the Stokes number for different values of Wi is presented in fig. 5. It is seen that the correlation dimension decreases from a value, which is realized in the limit of very small St, close to $D_2 = 2$ (corresponding to tracers homogeneously filling the whole space domain) to attain a minimum value of $D_2 \approx 1$ for $St \approx 1$. We remark that for very low particle inertia, the decrease of D_2 is quadratic in St (see inset of fig. 5), as it typically happens in correlated flows [40]. For even larger values of the Stokes number, D_2 grows to approach again the space filling value of 2 (expected for large inertia particles that are insensitive to the flow) in the limit of very large St. We find that the correlation dimension is weakly dependent on the Weissenberg number,

for the values of Wi explored here. The maximum relative difference, for fixed St, is found to not exceed 0.15. We can therefore conclude that small-scale clustering is a generic and quite effective phenomenon in elastic turbulence flows, producing, at its maximum, particle accumulation on quasi one-dimensional fractal sets. Our results are qualitatively similar to previous ones obtained in simulations of 2D smooth random flows [41].

3.4 Elastically driven turbophoresis

In this section we investigate the large-scale properties of the particle spatial distribution. Here, a motivation is provided by the observation that some form of modulation along the mean-shear direction (y) is already apparent from the visualizations of fig. 2. To analyze how this is related to the flow features, we introduce the particle number density field $\rho(\boldsymbol{x}, t)$ and focus on the profiles along the direction of inhomogeneity y of both ρ and flow statistics. For each considered quantity, the y-profile is obtained by averaging over the mean-flow direction x and time, which leaves a function of y only. We indicate profiles with $\langle(\ldots)\rangle$. Note that this type of average is related to the global one introduced in sect. 2 by

$$\overline{(\ldots)} = \frac{1}{L_0}\int_0^{L_0} \langle(\ldots)\rangle \mathrm{d}y.$$

Figure 6 presents the profiles of ρ (panel (a)) for three different Stokes numbers, as well as those of several flow related quantities (panels (b) and (c)), in a state of elastic turbulence (with $Wi = 23.9$ and $Re = 0.664$). All profiles are normalized by their, uniform, global average value to stress the deviations from it. We remark that $\langle u_y\rangle(y) = 0$ with very good accuracy in the numerics, as expected from symmetry considerations. We also note that the shown results are obtained by further averaging them over one forcing wavelength $\ell = LL_0 = \pi/2$. Comparing panels (a) and (b) of the figure, we see that, consistently with the previous analysis, particles are maximally concentrated where the longitudinally averaged Okubo-Weiss parameter $\langle Q\rangle(y)$ is minimum. Remark that here $\langle Q\rangle(y)$ is normalized by $Q^{rms}_{St=0}$ due to the fact that $\overline{Q}_{St=0} = 0$. Nevertheless, in such regions of minimal $\langle Q\rangle(y)$, the profile of the trace of the conformation tensor $\langle \mathrm{tr}(\boldsymbol{\sigma})\rangle(y)$ is now found to be minimum too. This apparently contradicts the observation made in sect. 3.2 that particles aggregate in regions of highly elongated polymers. This contradiction is solved by considering that profiles result from a spatial averaging procedure. Indeed, all information about the spatial structure along the longitudinal direction is lost in them, which are functions of the transversal direction only. This particularly applies to the information about the extent of vortices along x, from which particles are expelled, and about the orientation, with respect to x, of the separatrices, by which particles tend to be attracted and that colocate with high polymer elongation regions. While the profile $\langle Q\rangle(y)$ receives contributions only from the transverse fluctuating component of the velocity

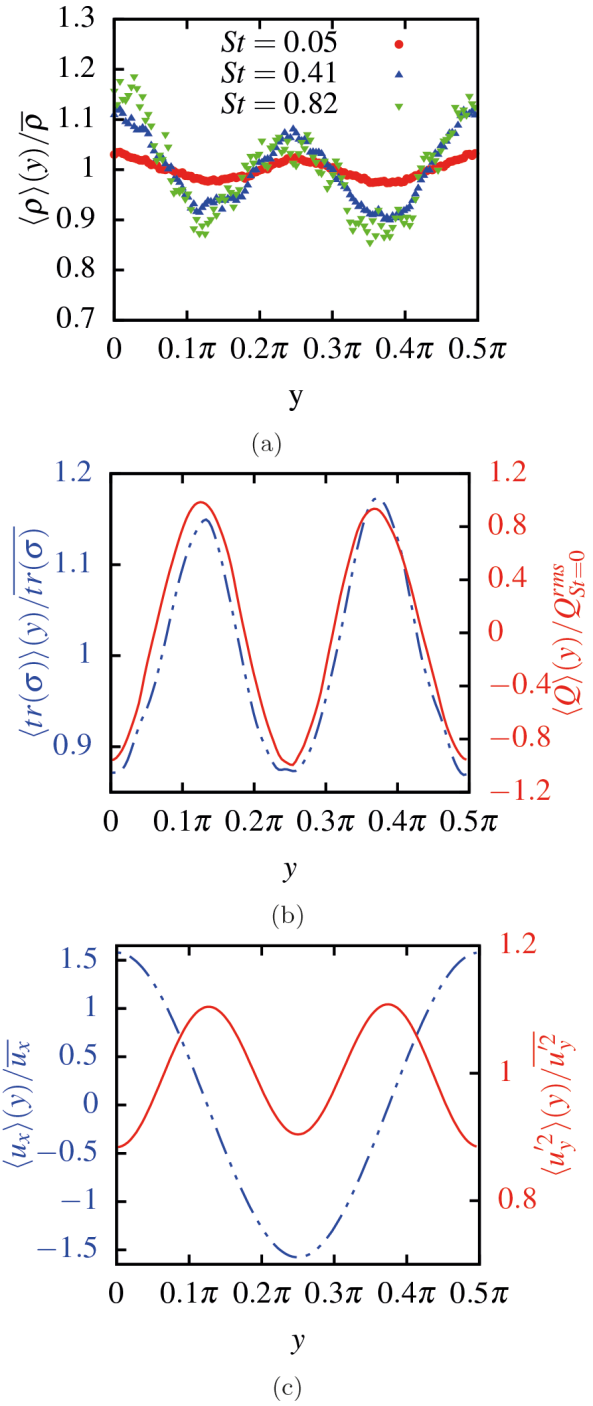

Fig. 6. (a) Particle number density profiles $\langle\rho\rangle(y)/\overline{\rho}$, normalized by the global mean uniform density ($\overline{\rho} = 1/L_0$), for three different Stokes numbers. (b) Normalized profile of the trace of the conformation tensor $\langle \mathrm{tr}(\boldsymbol{\sigma})\rangle(y)/\overline{\mathrm{tr}(\boldsymbol{\sigma})}$ (blue dashed line, left axis) and of Okubo-Weiss parameter $\langle Q\rangle(y)/Q^{rms}_{St=0}$ (red solid line, right axis). (c) Normalized profiles of the longitudinal velocity $\langle u_x\rangle(y)/\overline{u_x}$, where $\overline{u_x} = U$, (dashed blue line, left axis) and of the fluctuations of the shear-normal kinetic energy $\langle u_y'^2\rangle(y)/\overline{u_y'^2}$ (red solid line, right axis) of the fluid flow. The plots in (a)–(c) refer to statistically stationary conditions for $Wi = 23.9$, $Re = 0.664$. All the shown profiles are further averaged over the wavelength defining the periodicity of the mean flow $\ell = LL_0 = \pi/2$.

field, indeed $\langle Q\rangle(y) = -\partial_y^2\langle u_y'^2\rangle(y)$ (with prime indicating the fluctuation), the trace of the conformation tensor is dominated by the contribution of the mean flow, $\langle u_x\rangle(y)$, to polymer stretching and $\langle \mathrm{tr}(\sigma)\rangle(y)/\overline{\mathrm{tr}(\sigma)} \simeq \langle\sigma_{11}\rangle(y)/\overline{\sigma_{11}}$.

From the above discussion it should be clear that the large-scale inhomogeneities of ρ cannot be explained directly in terms of the averaged profiles. In fact, they are a manifestation of the turbophoresis phenomenon. In a nutshell, this corresponds to the migration of inertial particles from regions of high to regions of low eddy diffusivity that occurs in turbulent flows with non-homogeneous mean flow. Turbophoresis has been mainly studied in wall-bounded flows, because of their relevance for industrial and environmental applications related to particle deposition [11,42,43]. Interestingly, using the three-dimensional (3D) Newtonian turbulent Kolmogorov flow it was recently shown that turbophoretic segregation is independent of the presence of walls [13] (this was also confirmed in simulations employing a random inhomogeneous forcing [14]). Also in that case particles accumulate in regions of minimum turbulent diffusivity, but the spatial distribution of the latter with respect to the mean flow differs from the one found in geometrically confined flows [13].

The theoretical understanding of turbophoresis relies on statistical approaches. Models available in the literature are typically derived either from the Fokker-Planck equation obeyed by the probability density to find a particle at position $\boldsymbol{x}$ with velocity $\boldsymbol{v}$ at time t (as in [44]), or on the application of a decomposition into mean and fluctuating components, in the spirit of Reynolds averaging, in fluid momentum and particle mass conservation equations (as in [42]). Here we follow the second approach which, in spite of its more heuristic character, is perhaps more physically transparent; after a proper correspondence is made, both models provide the same results for what concerns the present discussion. We then write $f(\boldsymbol{x},t) = \langle f\rangle(y) + f'(\boldsymbol{x},t)$ for each quantity of interest $f(\boldsymbol{x},t)$, where the prime indicates the fluctuation. Defining as $\boldsymbol{J} = \rho\boldsymbol{v}$ the flux associated with the number density of particles, we have

$$\langle J_y\rangle(y) = \langle\rho\rangle(y)\langle v_y\rangle(y) + \langle\rho' v_y'\rangle(y) \tag{10}$$

for its component in the direction of inhomogeneity y. As is often done [42,45] we adopt a gradient diffusion model for the second term on the right-hand side of eq. (10):

$$\langle\rho' v_y'\rangle(y) = -D_p\frac{\mathrm{d}}{\mathrm{d}y}\langle\rho\rangle(y), \tag{11}$$

where D_p is the diffusion coefficient of the inertial particles. This is typically assumed to be close to that of fluid tracers (*i.e.*, the eddy diffusion coefficient) D_f, which is completely justified only in the limit of vanishingly small Stokes number. Estimating D_f dimensionally, one has:

$$D_p \approx D_f \approx \tau_c\langle u_y'^2\rangle(y), \tag{12}$$

where τ_c is a correlation time associated with the fluid flow. We expect it to be proportional to $\tau_{\dot\gamma}$ (eq. (5)), so that $\tau_{\dot\gamma}/\tau_c = a$ with a some constant of order 1. Still in the limit of $\tau_p \to 0$, using $\boldsymbol{v} \simeq \boldsymbol{u} - \tau_p(\partial_t\boldsymbol{u} + \boldsymbol{u}\cdot\boldsymbol{\nabla}\boldsymbol{u})$, the turbophoretic velocity in eq. (10) can be expressed as

$$\langle v_y\rangle(y) = -\tau_p\frac{\mathrm{d}}{\mathrm{d}y}\langle u_y'^2\rangle(y). \tag{13}$$

Inserting eq. (11), with (12), and eq. (13) into eq. (10), for the fluxless steady state (*i.e.* $\langle J_y\rangle(y) = 0$) we finally obtain:

$$\langle\rho\rangle(y) \sim \langle u_y'^2\rangle^{-\alpha}(y), \tag{14}$$

giving the relation between the inhomogeneities of the particle distribution and those of fluid velocity fluctuations. In this expression the exponent $\alpha = \tau_p/\tau_c = aSt$ controls the amplitude and shape of the spatial modulation of the particle density transversal profile.

The numerical results, shown in fig. 7, are in quite good agreement with the expectation of eq. (14), providing quantitative support to the claim that the large-scale inhomogeneities of the particle distribution are controlled by a turbophoretic mechanism. The small asymmetries observable in $\langle\rho\rangle(y)$ are due to the very slow convergence of particle statistics. As in fig. 6, the results shown here are obtained by further averaging profiles over one forcing wavelength. The exponent α, measured by a fitting procedure, is found to increase with the Stokes number and to approach $\alpha \simeq 1$ for $St \approx 1$ or larger (fig. 8). The growth of α with St means that the amplitude of large-scale modulations of $\langle\rho\rangle(y)$, and hence the importance of turbophoresis, grows with increasing particle inertia. For the smallest values of St, α is found to linearly grow with St, with a value of the fitted proportionality constant $a = 4.4$ (see the dashed black line in fig. 8). Hence, in this range of small particle inertia the numerical results are commensurate with the model prediction $\alpha \sim St$ valid in the limit of vanishingly small St. For larger St, the data are no longer described by this linear relation, with α tending to saturate to 1. To account for this behavior we follow [42] and [46], where it was suggested that the shear-normal particle kinetic energy is different from the fluid one, being proportional to it through a St-dependent coefficient κ. The turbophoretic velocity in eq. (13) should then be modified as follows:

$$\langle v_y\rangle(y) = -\kappa\tau_p\frac{\mathrm{d}}{\mathrm{d}y}\langle u_y'^2\rangle(y), \tag{15}$$

where $\kappa = 1/(1+\tau_p/\tau_c)$ [42]. Reasoning as before, we obtain a fluxless steady solution like the one in eq. (14) but with

$$\alpha = \frac{aSt}{1+aSt}\,. \tag{16}$$

Remark that, from this, $\alpha \simeq aSt$ for $St \simeq 0$ and $\alpha \to 1$ for very large St. This modified Stokes dependence captures quite well the behavior of the exponent α in a considerably broader range of St extending to unity and beyond, as shown in fig. 8 (solid black line, with $a = 4.4$ as for the linear behavior). For even larger values of St we were unable to obtain satisfactorily converged particle statistics. We note that these results weakly depend on Wi.

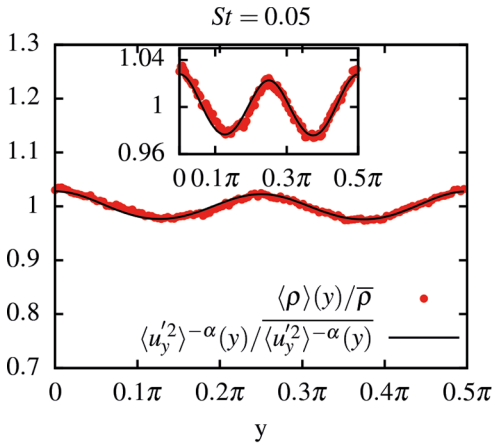

(a)

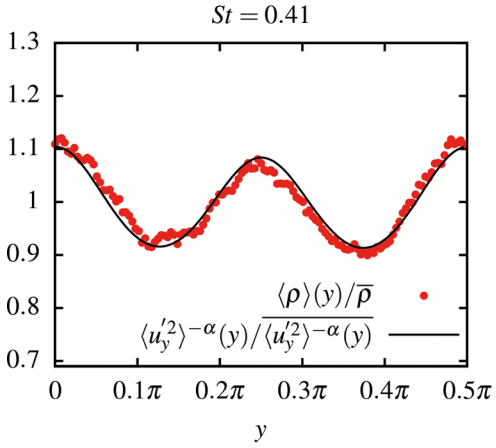

(b)

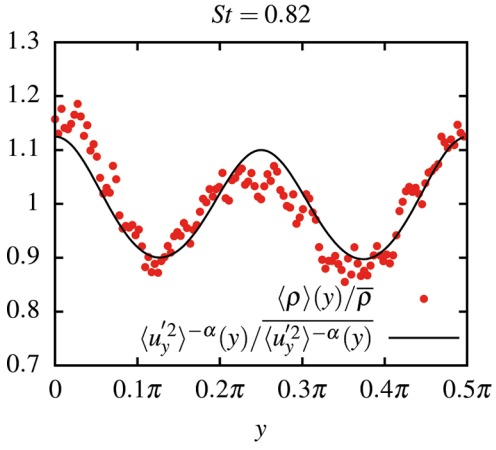

(c)

Fig. 7. Comparison of normalized particle number density profiles $\langle\rho\rangle(y)/\overline{\rho}$ (red points) with the normalized profiles of transversal velocity fluctuations $\langle u_y'^2\rangle^{-\alpha}(y)/\overline{\langle u_y'^2\rangle^{-\alpha}(y)}$ (black solid line) for $Wi = 23.9$, $Re = 0.664$ and different values of St (increasing from top to bottom). The values of the exponents obtained from a best fit are $\alpha = 0.229 \pm 0.029$ (a), $\alpha = 0.839 \pm 0.149$ (b), $\alpha = 1 \pm 0.309$ (c). The inset in (a) is a zoom around $\langle\rho\rangle(y)/\overline{\rho} = 1$. All the shown profiles are further averaged over the wavelength defining the periodicity of the mean flow $\ell = LL_0 = \pi/2$.

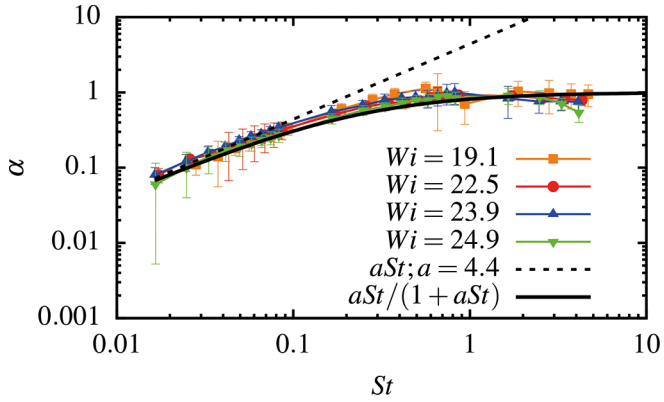

Fig. 8. Exponent α as a function of St and for different Weissenberg numbers. The black dashed line represents the linear prediction in the limit of small St. The black solid line represents the modified non-linear prediction; $a = 4.4$ is obtained by a best fit.

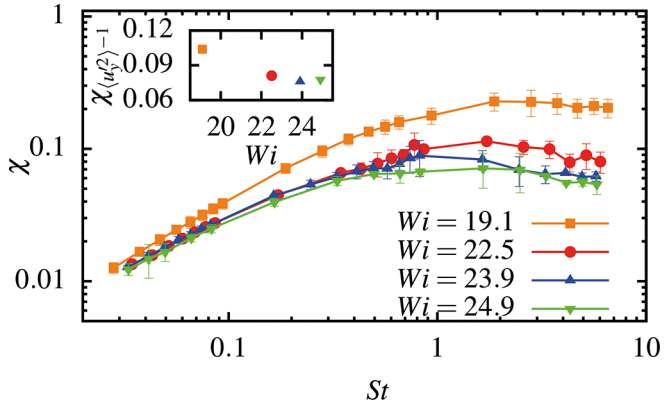

Fig. 9. Root-mean-square (rms) relative deviation χ of $\langle\rho\rangle$ from the mean uniform distribution $\overline{\rho}$ as a function of St and for different Weissenberg numbers. Here temporal averages are performed over 80 independent realizations corresponding to different instants of time separated by an interval larger than the typical flow time scale. The inset shows the parameter $\chi_{\langle u_y'^2\rangle^{-1}}$ computed from the rms relative deviation of $\langle u_y'^2\rangle^{-1}$ from the mean uniform value $\overline{\langle u_y'^2\rangle^{-1}}$, *i.e.* $\sigma_{\langle u_y'^2\rangle^{-1}}/\overline{\langle u_y'^2\rangle^{-1}}$, as a function of Wi.

To quantitatively assess the overall effect of turbophoresis, as in [13], we measure the rms relative deviation of the mean particle density profile $\langle\rho\rangle(y)$ from the uniform distribution $\overline{\rho} = 1/L_0$, defined as

$$\chi \equiv \frac{\sigma_{\langle\rho\rangle(y)}}{\overline{\rho}} = \left[\frac{1}{L_0}\int_0^{L_0}\left(1 - \frac{\langle\rho\rangle(y)}{\overline{\rho}}\right)^2 \mathrm{d}y\right]^{\frac{1}{2}}, \qquad (17)$$

where $\sigma_{\langle\rho\rangle(y)}$ is the standard deviation of $\langle\rho\rangle(y)$. The global parameter χ as a function of Stokes for different Wi numbers is presented in fig. 9. Consistently with the behavior of α, we find that χ grows with St and eventually reaches an approximately constant value for $St \geq 1$. In the limit of $St \to \infty$, we would expect χ to be a decreasing function of St, due to the fact that, practically, very heavy particles should not interact with the flow field. However,

this point could not be verified within this study, due to finite statistics associated with the difficulty to attain large enough Stokes numbers. The approximately constant behavior of χ for $St \geq 1$ appears nevertheless reasonable from its definition, considering that in the same range of Stokes numbers the exponent α characterizing $\langle\rho\rangle(y)$ is at a plateau value.

Finally, we observe that χ displays some dependency on Wi, which becomes more evident as St increases. Indeed, as seen from fig. 9, χ decreases with increasing Wi, suggesting that the large-scale accumulation of particles (quantified by χ) decreases with increasing polymer elasticity. This trend can be possibly connected to the changes in $\langle u_y'^2\rangle(y)$ at growing Wi, which correspond to an increase of its mean accompanied by a weak reduction of its peak-to-peak excursions. Indeed, if we focus on the region $St = O(1)$ where the effect of varying Wi is most important, and we substitute $\langle\rho\rangle(y)$ with $\langle u_y'^2\rangle^{-1}(y)$ (notice that $\alpha \simeq 1$ for $St = O(1)$) in the expression of χ, we then should have a decrease of its plateau value with Wi. As shown in the inset of fig. 9, the computation of $\chi_{\langle u_y'^2\rangle^{-1}}$, *i.e.* the one based on $\langle u_y'^2\rangle^{-1}(y)$ confirms this expectation.

4 Conclusions

The small- and large-scale inhomogeneities of the distribution of heavy inertial particles passively transported by a 2D elastic turbulence flow with (Kolmogorov) sinusoidal mean shear [22,23,25] have been investigated by means of direct numerical simulations.

A strong correlation bewteen the particle distribution and the polymer (square) elongation field was detected, with large particle concentrations occurring along thin highly elastic filamentary structures. Since the interaction between polymers and particles is not direct in the adopted model dynamics, but rather mediated by the fluid flow, it has been possible to interpret such a phenomenon in terms of the preferential concentration of particles outside vortices, in strain-dominated regions where, in turn, polymers are efficiently stretched. The statistical features of small-scale clustering were further addressed measuring the correlation dimension of the fractal sets on which particles accumulate, *i.e.* the scaling exponent of the probability density to find particle pairs at small distances. The analysis revealed particularly effective clustering for Stokes numbers of order unity, for which D_2 decreases to approximately 1, pointing to the aggregation of particles on almost one-dimensional structures. The considered statistics display only rather weak dependence on the Weissenberg number, in the range of parameters explored.

At large scales, a turbophoretic mechanism associated with the gradients of eddy diffusivity was found to be responsible of segregation, as in Newtonian fluids at high Reynolds number [11–14]. Indeed, the particle spatial distribution is strongly linked to the structure of the mean and fluctuating components of the fluid velocity, with maxima in correspondence to the minima of the shear-normal (elastic) turbulence intensity. A detailed analysis allowed us to measure the exponent characterizing the relation between the mean particle density profile and turbulence intensity in the direction transversal to the mean flow. Differently from the case of the 3D Newtonian turbulent Kolmogorov flow, this exponent was found to depend on particle inertia, *i.e.* on the Stokes number. Such a dependence resulted to be non-linear in St and could be explained by adapting previous theoretical approaches [42, 44] to construct a simple model by means of a Reynolds averaging procedure. A similar non-linear dependence is also reflected in the overall intensity of the turbophoresis phenomenon, quantified by the global parameter χ accounting for the rms deviation of the particle distribution, relative to the uniform one. This quantity shows some negative dependence on the Weissenberg number, suggesting a reduction of segregation for larger values of Wi, a feature that is likely related to the progressively (with growing Wi) less inhomogeneous character of transversal fluid velocity fluctuations.

These results were obtained adopting the constant viscosity Oldroyd-B model of viscoelasticity. Despite it is known that linear elasticity models, such as Oldroyd-B, typically underestimate the experimentally measured elastic stresses [47], it has been argued that the main features of elastic turbulence are quite independent of the rheological model details [22, 24, 29, 33]. Nevertheless, the effect of the latter on particle dynamics might not be unimportant. In particular, rheological models accounting for shear-dependent viscosity effects (such as FENE models) could bring in additional dynamical couplings between the flow and the particles [48]. One could indeed expect that, *e.g.*, in a shear-thinning fluid the varying effective viscosity would reduce the drag force experienced by the particles in the regions of the flow where polymers are maximally stretched, and this might in turn affect the particle unmixing properties. It is a subject that deserves future investigations in order to assess to what extent the phenomenology described in this paper would apply.

The research leading to these results has received funding from European COST Action MP1305 “Flowing matter”.

Author contribution statement

All the authors contributed to the preparation of the paper. They have all read and approved the final manuscript.

References

1. A. Groisman, V. Steinberg, Nature **405**, 53 (2000).
2. A. Groisman, V. Steinberg, Nature **410**, 905 (2001).
3. L. Pan, A. Morozov, C. Wagner, P. Arratia, Phys. Rev. Lett. **110**, 174502 (2013).
4. A. Souliès, J. Aubril, C. Castelain, T. Burghelea, Phys. Fluids **29**, 083102 (2017).
5. P.C. Sousa, F.T. Pinho, M.A. Alves, Soft Matter **14**, 1344 (2018).

6. B. Traore, C. Castelain, T. Burghelea, J. Non-Newton. Fluid Mech. **223**, 62 (2015).
7. W.M. Abed, R.D. Whalley, D.J.C. Dennis, R.J. Poole, J. Non-Newton. Fluid Mech. **231**, 68 (2016).
8. R.J. Poole, B. Budhiraja, A.R. Cain, P.A. Scott, J. Non-Newton. Fluid Mech. **177**, 15 (2012).
9. J. Mitchell, K. Lyons, A.M. Howe, A. Clarke, Soft Matter **12**, 460 (2016).
10. K.D. Squires, J.K. Eaton, Phys. Fluids A **3**, 1169 (1991).
11. F. Picano, G. Sardina, C.M. Casciola, Phys. Fluids **21**, 093305 (2009).
12. G. Sardina, P. Schlatter, L. Brandt, F. Picano, C.M. Casciola, J. Fluid Mech. **699**, 50 (2012).
13. F. De Lillo, M. Cencini, S. Musacchio, G. Boffetta, Phys. Fluids **28**, 035104 (2016).
14. D. Mitra, N.E.L. Haugen, I. Rogachevskii, Eur. Phys. J. Plus **133**, 35 (2018).
15. J. Bec, Phys. Fluids **15**, L81 (2003).
16. E. Calzavarini, M. Kerscher, D. Lohse, F. Toschi, J. Fluid Mech. **607**, 13 (2008).
17. F. Toschi, E. Bodenschatz, Annu. Rev. Fluid Mech. **41**, 375 (2009).
18. F. De Lillo, G. Boffetta, S. Musacchio, Phys. Rev. E **85**, 036308 (2012).
19. A. Nowbahar, G. Sardina, F. Picano, L. Brandt, J. Fluid Mech. **732**, 706 (2013).
20. E. Afik, V. Steinberg, Nat. Commun. **8**, 468 (2017).
21. B. Bird, C.F. Curtiss, R.C. Armstrong, O. Hassager, *Dynamics of Polymeric Fluids* (Wiley, New York, 1987).
22. S. Berti, A. Bistagnino, G. Boffetta, A. Celani, S. Musacchio, Phys. Rev. E **77**, 055306(R) (2008).
23. S. Berti, G. Boffetta, Phys. Rev. E **82**, 036314 (2010).
24. E.L.C. VI, M. Plan, A. Gupta, D. Vincenzi, J.D. Gibbon, J. Fluid Mech. **822**, R4 (2017).
25. G. Boffetta, A. Celani, A. Mazzino, A. Puliafito, M. Vergassola, J. Fluid Mech. **523**, 161 (2005).
26. M.R. Maxey, J.J. Riley, Phys. Fluids **26**, 883 (1983).
27. R. Sureshkumar, A.N. Beris, J. Non-Newton. Fluid Mech. **60**, 53 (1995).
28. T. Vaithianathan, L.R. Collins, J. Comput. Phys. **187**, 1 (2003).
29. A. Fouxon, V. Lebedev, Phys. Fluids **15**, 2060 (2003).
30. E. De Angelis, C.M. Casciola, R. Piva, Physica D **241**, 297 (2012).
31. M.Q. Nguyen, A. Delache, S. Simoëns, W.J.T. Bos, M. El Hajem, Phys. Rev. Fluids **1**, 083301 (2016).
32. Y. Jun, V. Steinberg, Phys. Rev. Fluids **2**, 103301 (2017).
33. A. Gupta, R. Pandit, Phys. Rev. E **95**, 033119 (2017).
34. M.R. Maxey, J. Fluid Mech. **174**, 441 (1987).
35. J. Bec, L. Biferale, G. Boffetta, A. Celani, M. Cencini, A. Lanotte, S. Musacchio, F. Toschi, J. Fluid Mech. **550**, 349 (2006).
36. A. Okubo, Deep-Sea Res. **17**, 445 (1970).
37. J. Weiss, Physica D **48**, 273 (1991).
38. K. Gustavvson, B. Mehlig, Adv. Phys. **65**, 1 (2016).
39. P. Grassberger, I. Procaccia, Phys. Rev. Lett. **50**, 346 (1983).
40. G. Falkovich, A. Fouxon, M.G. Stepanov, Nature **419**, 151 (2002).
41. J. Bec, J. Fluid Mech. **528**, 255 (2005).
42. M. Caporaloni, F. Tampieri, F. Trombetti, O. Vittori, J. Atmos. Sci. **32**, 565 (1975).
43. J.W. Brooke, K. Kontomaris, T. Hanratty, J.B. McLaughlin, Phys. Fluids A **4**, 825 (1992).
44. S. Belan, I. Fouxon, G. Falkovich, Phys. Rev. Lett. **112**, 234502 (2014).
45. A. Guha, J. Aerosol Sci. **28**, 1517 (1997).
46. J.O. Hinze, *Turbulence: An Introduction to its Mechanism and Theory* (McGraw-Hill, New York, 1959).
47. Y. Liu, V. Steinberg, EPL **90**, 44002 (2010).
48. A. Nowbahar, G. Sardina, F. Picano, L. Brandt, J. Fluid Mech. **732**, 706 (2013).